



34 applications (Van et al., 2008). The unique advantages of AVHRR sensors is their long history
35 dating back to the 1980s and thus enabling long-term analyses at climate-relevant time scales
36 that cannot be covered by other satellites. However, AVHRR data are rarely used at the full
37 spatial resolution for global monitoring due to the limited data availability (Pouliot et al., 2009;
38 Fontana et al., 2009). Instead, the Global Area Coverage (GAC) AVHRR dataset with a reduced
39 spatial resolution is generally employed in long-term studies at a global or regional perspective
40 (Hori et al., 2017; Delbart et al., 2006; Stöckli et al., 2004; Moulin et al., 1997).

41 However, there are several known problems with the geo-location of AVHRR GAC data,
42 which have a profound impact on their application. (1) The drift of the spacecraft clock results
43 in errors in the along-track direction (Devasthale et al., 2016). Generally, an uncertainty of 1
44 second approximately induces an error of 8 km in this direction. (2) Satellite orientation and
45 position uncertainties influence the projection of the satellite geometry to the ground, which
46 leads to errors in both along-track and across-track directions. (3) Earth surface elevation
47 aggravates distortions in the across-track direction (Fontana et al., 2009). Without navigation
48 corrections, the spatial misplacement of the GAC scene caused by these factors can be up to
49 25-30 km occasionally (Devasthale et al., 2016).

50 For geocoding of AVHRR data, a two-step approach is usually used: 1) geocoding based
51 on orbit model, ephemeris data, and time of onboard clock (Van et al., 2008), achieving an
52 accuracy within 3-5 km depending on the accuracy of orbit parameters and model (Khlopenkov
53 et al., 2010); 2) using any kind of ground control points (GCPs) (e.g., road or river intersections,
54 coastal lines) to improve geocoding (Takagi, 2004; Van et al., 2008). Additionally, in order to
55 eliminate the ortho-shift caused by elevations, an orthorectification would be needed (Aguilar
56 et al., 2013; Khlopenkov et al., 2010). The dataset used in this study is from the ESA (European
57 Space Agency) cloud CCI (Cloud Climate Change Initiative) project, which has corrected clock
58 drift errors by coregistration of AVHRR GAC data with a reference dataset, and showed
59 improved navigation by fitting the data to coastal lines.

60 Unlike the Local Area Coverage (LAC) data with a full spatial resolution of AVHRR, GAC
61 data are sampled on board the satellite in real-time to generate reduced resolution data (Kidwell,
62 1998). This is achieved by averaging values from four out of five pixel samples along a scan
63 line and eliminating two out of three scan lines, resulting in a spatial resolution of $1.1 \text{ km} \times 4$
64 km along the scan line with a 3 km distance between pixels across the scan line. Therefore, the
65 nominal size of a GAC pixel is $3 \text{ km} \times 4.4 \text{ km}$. It is important to note that the spatial resolution
66 of GAC data also depends on the satellite zenith angle (SatZ). Because of the large swath width,
67 the spatial resolution of LAC decreases to 2.4 km by 6.9 km at the edge of the swath (D'Souza
68 et al., 1994). With the selection process for GAC, the GAC resolution is also much worse than
69 4 km . Furthermore, the onboard resampling process of GAC data makes the orthorectification
70 not feasible, which results in lowering of geolocation accuracy in the across-track direction.
71 The final quality of AVHRR GAC data has not been quantified and we, therefore, make an
72 attempt to assess their geolocation accuracy, particularly over terrain areas.



73 There are generally three approaches to assess the non-systematic geometric errors of
74 satellite images: (1) the coastline crossing method (CCM) which detects the coastline in the
75 along-track and across-track directions through a cubic polynomial fitting (Hoffman et al.,
76 1987); (2) the land-sea fraction method (LFM) which develops a linear radiance model as a
77 function of land-sea fraction, land and sea radiance, and then finds the minimum difference
78 between model-simulated and instrument-observed radiance by shifting the pixels in along-
79 track and across-track directions; (3) the coregistration method which computes the difference
80 or similarity relative to a reference image (Khlopenkov et al., 2010). The abilities of these
81 methods in characterizing the geometric errors are limited to certain conditions. The CCM is
82 subject to the structure of coastline. Although the LFM works better on complex coastlines but
83 depends on the accuracy of the land-sea model. The coregistration method is usually applied to
84 high-resolution visible and infrared images (Wang et al., 2013; Wolfe et al., 2013). When it
85 comes to coarse resolution data with several kilometers, the main difficulty arises from false
86 detection due to the effect of mixed pixels. The geometric accuracy is important as even small
87 geometric errors can lead to significant noises on the retrieval of surface parameters, such as
88 NDVI, LAI, and albedo, which mask the reality or bias the final results and conclusions
89 (Khlopenkov et al., 2010; Arnold et al., 2010). For instance, anomalous NDVI dynamics during
90 the regeneration phase of forest fire-burnt areas can be explained by the imprecise geolocation
91 of the data set used (Alcaraz-Segura et al., 2010). Therefore, it is critical to develop a rigorous
92 geometric accuracy assessment method in order to ensure the effectiveness of AVHRR GAC
93 data in the generation of climate data records (CDR) (Khlopenkov et al., 2010; Van et al., 2008).

94 Based on the idea of the coregistration method, this study proposes a method named
95 Correlation-based Patch Matching Method (CPMM), which is capable of quantifying the
96 geometric accuracy of coarse resolution satellite data available as fundamental climate data
97 records (FCDR) for global applications (Hollmann et al., 2013). We show the procedure based
98 on AVHRR GAC data, which are compiled for the ESA CCI cloud project (Stengel et al., 2017)
99 and are now also used for the ESA CCI+ snow project. The assessment is conducted at the sub-
100 pixel level and not affected by the mixed pixel problem. This method is applied to some test
101 data from NOAA-17, MetOp-A, and MetOp-B, respectively. Furthermore, the potential factors
102 that cause geometric distortions are explored and discussed. Although the band-to-band
103 registration (BBR) accuracy assessment is an important aspect for such multi-spectral images,
104 it is not a focus of this study, since the BBR accuracy of AVHRR has been comprehensively
105 evaluated by a previous study (Aksakal et al., 2015).

106 **2 Data and geographical regions of interest**

107 **2.1 Satellite data**

108 AVHRR is a multipurpose imaging instrument aboard on the NOAA satellite series since
109 1978 and the Meteorological Operational Satellites (MetOp) operated by EUMETSAT since



110 2006, delivering daily information of the Earth in the visible, near-infrared, and thermal
111 wavelengths. They provide observations from 4 to 6 spectral bands, depending on the
112 generation of AVHRR sensors. This study only focuses on the AVHRR GAC data observed by
113 NOAA-17 (AVHRR-3 generation), MetOp-A, and MetOp-B. The spectral characteristics of the
114 AVHRR sensors on board these three platforms are the same and summarized in Table 1. Since
115 the spatial resolution of AVHRR GAC data is often considered to be 4 km (Fontana et al., 2009),
116 the analysis in this study was conducted at the 4 km level using the data acquired on August 13,
117 2003 for NOAA-17 and March 12, 2017 for MetOp-A and MetOp-B.

118 **Table 1.** Spectral characteristics of AVHRR sensors

Band	Wavelength (μm)	Application
1	0.58–0.68 (VIS)	Cloud mapping, vegetation and surface characterization
2	0.72–1.00 (NIR)	Vegetation mapping, water body detection
3a*	1.58–1.64 (MIR)	Snow and Ice classification
3b*	3.55–3.93 (MIR)	Cloud detection, Sea/Land surface temperature,
4	10.30–11.30 (TIR)	Cloud detection, Sea/Land surface temperature,
5	11.50–12.50 (TIR)	Cloud detection, Sea/Land surface temperature

119 *Note: Channel 3a is only used continuously on NOAA-17 and MetOp-A. On-board MetOp-B channel 3a was only
120 active during a limited time span.

121 From a standpoint of geometric accuracy assessment, the reflectances in band 1 and 2 were
122 employed in this study. However, these two bands are not only affected by the atmosphere but
123 also by the earth surface anisotropy characterized by the bidirectional reflectance distribution
124 function (BRDF) (Cihlar et al., 2004). Given the fact that BRDF effects can be reduced through
125 the calculation of vegetation indices such as NDVI (Lee & Kaufman, 1986), the NDVI is
126 employed in this study, which is derived from the reflectance in band 1 and 2 according to
127 Equation (1).

128
$$NDVI = \frac{R_2 - R_1}{R_2 + R_1} \quad (1)$$

129 where R_1 and R_2 refer to the reflectance in band 1 and 2, respectively. It is important to note
130 that during the process of generating NDVI, the atmospheric and BRDF corrections were not
131 performed. But it is expected that such effects originating from these omissions are of minor
132 influence, because the method of this study is based on correlation analysis and does not rely
133 on absolute values of NDVI. Another advantage of using NDVI is that it has higher contrast
134 between different land cover types, such as vegetation/no-vegetation, snow/no-snow, etc.
135 Furthermore, in order to investigate the effect of off-nadir viewing angle on geometric accuracy,
136 the SatZ data of AVHRR were also extracted.

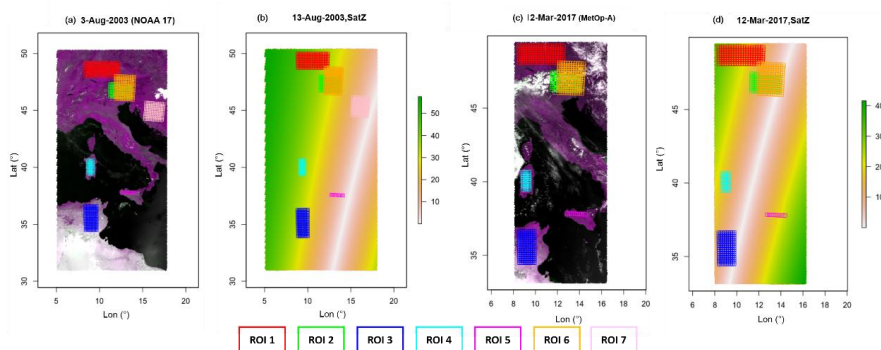
137 Ideally, the referenced data in geometric quality assessment should meet the required
138 accuracy of 1/3 field of view (FOV) (WMO and UNEP, 2006), and also satisfy the accuracy



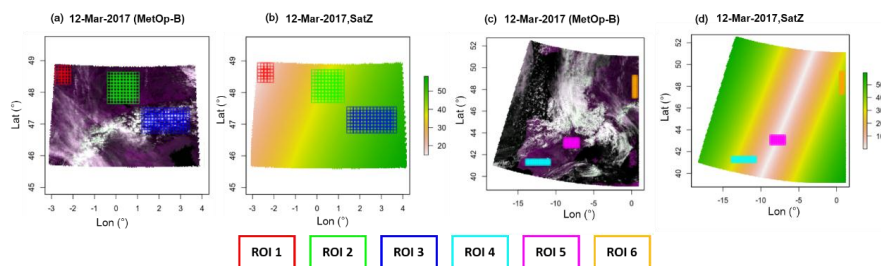
139 requirement of an order of magnitude better than one-tenth of the image spatial resolution
140 (Aksakal, 2013), which means 400 m for the AVHRR GAC data. The NDVI provided by
141 MOD13A1 V006 product was introduced as a source of reference data to perform the geometric
142 quality assessment, because the sub-pixel accuracy of MODIS product is sufficient to satisfy
143 this requirement (Wolfe et al., 2002). The high geolocation accuracy of MODIS products was
144 achieved by using the most advanced data processing system, which has updated the models of
145 spacecraft and instrument orientation several times since launch. Consequently, the various
146 geolocation biases resulted from instrument effects and sensor orientation are removed (Wolfe
147 et al., 2002). The NDVI data with the date corresponding to that of AVHRR GAC data, were
148 obtained from the Level-1 and Atmosphere Archive & Distribution System (LAADS)
149 Distributed Active Archive Center (DAAC) (<https://ladsweb.modaps.eosdis.nasa.gov/>) with
150 the sinusoidal projection at a spatial resolution of 500 m and a temporal resolution of 16-day.
151 The detailed description of the MOD13A1 V006 product can be found in Didan (2015).

152 2.2 Geographical regions of interest

153 The purpose of this study is not only to assess the geolocation accuracy of 4 km AVHRR
154 GAC data, but also to explore the potential impact factors related to geolocation accuracy.
155 Therefore, the investigations were made at different latitudes and longitudes, at different
156 locations with different SatZ, for different land covers, as well as different topographies. The
157 swaths covering parts of Europe (including the alpine mountain) and Africa were used since
158 they fit the study needs (Fig. 1). Investigations were based on six regions of interest (ROI) as
159 shown in Figs. 1 and 2. The ROIs from 1 to 6 enable us to investigate the geolocation accuracy
160 at different SatZ, topography, as well as latitudes and longitudes. Their locations and extents
161 are consistent for the scenes from NOAA-17 and MetOp-A (Fig. 1), which enables the
162 comparison of geolocation accuracy between these two sensors. The size of ROI was attempted
163 to be set as large as possible in order to get more significant and comprehensive results. On the
164 other hand, areas covered by cloud and water have to be avoided, resulting in the different sizes
165 of these ROIs. Half of the ROIs (ROIs 2, 4, 6) serve as a good example for a typical
166 mountainous areas on Earth. The other half of ROIs (ROIs 1, 3, 5), on the other hand, mainly
167 cover relatively flat areas. Since the NOAA-17 scene was almost unaffected by cloud, another
168 ROI (ROI 7) was selected to check the geolocation accuracy at nadir. The MetOp-B scene was
169 influenced by cloud but served as a good example to illustrate the combined effect of
170 topography and large SatZ (Fig. 2). Although there are also 6 ROIs selected, their sizes and
171 extents are totally different from the above two scenes. In order to include the terrain area, two
172 subsets were used (Figs. 2a and c). Each grid in the ROI represents the minimum unit (namely
173 the patch) based on which we conduct the geometric quality analysis.



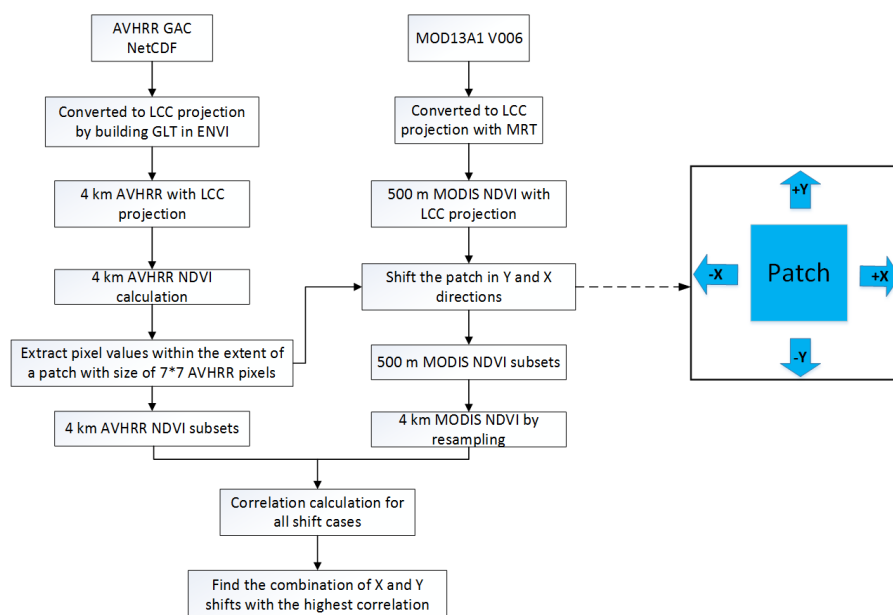
174
 175 **Figure 1.** The study area and the distribution of ROIs. (a) and (c) are the composite maps of bands 2-1-
 176 1 of AVHRR GAC data on August 13, 2003 and March 12, 2017, respectively. (b) and (d) are their
 177 corresponding SatZ, respectively.



178
 179 **Figure 2.** The study area and the distribution of ROIs on March 12, 2017. (a) and (c) are the composite
 180 maps of bands 2-1-1 subset 1 and 2, respectively. (b) and (d) are their corresponding SatZ, respectively.

181 3 Methodology

182 The assessment was performed by comparing the AVHRR GAC scenes with geo-located
 183 reference data, i.e. MOD13A1 (V006). An approach named Correlation-based Patch Matching
 184 Method (CPMM) is proposed to find the best match between small image patches taken from
 185 the reference images and the AVHRR GAC images. This method is expected to be more suitable
 186 for the geometric accuracy assessment of coarse resolution images than the current methods,
 187 i.e. the CGM, LFM, and co-registration using shorelines. Because it is not limited to a certain
 188 landmark such as a lake or sea shoreline, and thus enables a more comprehensive assessment
 189 over different areas in the satellite scene. Moreover, this method does not suffer from errors
 190 caused by false detection due to the effect of mixed pixels because it is applied directly on the
 191 pixel values. The framework of CPMM is shown in Fig. 3, and the detailed description of this
 192 method is provided below.



193

194

Figure 3. Flowchart of the Correlation-based Patch Matching Method (CPMM).

195 3.1 Satellite data processing

196 The AVHRR GAC data set is stored in a Network Common Data Format (NetCDF), with
 197 latitude and longitude assigned to each pixel. In order to achieve a higher accuracy of image
 198 matching, the data need to be reprojected. The AVHRR GAC scene was reprojected into the
 199 Lambert Conformal Conic (LCC) projection by building the Geographic Lookup Table (GLT)
 200 using the latitude and longitude data in ENVI. The spatial resolution of the AVHRR GAC map
 201 in the LCC projection is 4 km. Based on the reprojected data, the NDVI was calculated using
 202 the band combinations as indicated by Eq. (1). Similarly, the NDVI band of MOD13A1 in the
 203 HDF format was extracted and converted to LCC projection from its raw sinusoidal projection
 204 using the MODIS Reprojection Tool (MRT). The nearest neighbor (NN) resampling scheme
 205 was employed in this procedure. The spatial resolution of the MODIS NDVI in the LCC
 206 projection is 500 m. Thus, the geometric assessment is performed at the 4 km resolution of
 207 AVHRR NDVI based on the 500 m MODIS NDVI data.

208 3.2 Patch matching and geometric assessment

209 In the process of matching the AVHRR GAC data with reference MODIS data, a patch
 210 size of 7×7 AVHRR pixels (corresponding to approximately $28 \text{ km} \times 28 \text{ km}$) was used. These
 211 patches were distributed in each ROI as shown in Figs. 1 and 2, with an interval of 4 pixels in
 212 the along-track (Y-) and across-track (X-) direction. The sizes of the patch and interval were
 213 determined based on the following aspects: the size of the patch should contain enough pixels
 214 to support a robust correlation estimation, but at the same time, should not be too large in order



215 to investigate the potential influencing factors related to the geometric accuracy, and get enough
216 results from these patches to attain a more significant and comprehensive conclusion. Similarly,
217 the size of the interval should enable the disparity between different patches on one hand and
218 on the other hand a large number of patches within the extent of each ROI. The chosen size has
219 proven to be most ideal for these criteria during the test of different patch size.

220 For each patch in the ROI, the AVHRR GAC data within the patch were extracted. Then
221 the patch was shifted in the Y- and X-direction as indicated by the blue arrows in Fig. 3. Shifts
222 were conducted stepwise in order to achieve sub-pixel accuracy, beginning with only 500 m
223 and adding up to 8 km (i.e., ± 2 pixels) at a step of 500 m (equivalent to the MODIS pixel size)
224 in any direction of Y- and X-combination. Consequently, 33×33 combinations of X- and Y-
225 shifts have been simulated. For each shift, the MODIS NDVI pixels within the extent of the
226 patch were extracted and aggregated to 4 km by spatial averaging. Afterwards, the correlation
227 between the 4 km rescaled MODIS NDVI and the 4 km AVHRR NDVI was calculated for each
228 shift in X- and Y-direction. The displacement of one patch was indicated by the shift
229 combination with the best correlation, which means the geolocation accuracy of the patch. In
230 this way, the geolocation errors were transformed into the across-track and along-track
231 directions at the sub-pixel level for correlation with possible error sources.

232 It is expected that the results from each patch are different. Therefore, the general accuracy
233 of each ROI was determined by summarizing the measured shifts of each respective patch
234 statistically. Here, the histogram was employed to show the distribution of geometric errors in
235 the across-track and along-track directions. And the quantitative indexes, such as the number
236 of patches, their mean and standard errors, were calculated. The averaging is expected to reduce
237 the uncertainties caused by random factors and produce accurate shift measurement estimates
238 (Bicheron et al., 2011). The final shifts of the scene were calculated by averaging the measured
239 shifts of all patches on the scene.

240 **3.3 Influence factor**

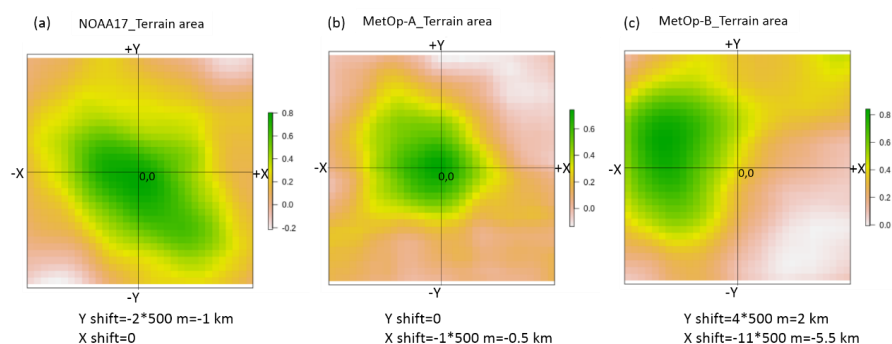
241 The influence of potential variables on the geometric accuracy was studied, including
242 SatZ, topography, latitudes, and longitude. To achieve this, the information of these factors were
243 also extracted for each patch on the scene. The geometric errors induced by SatZ were
244 highlighted by checking the relationship between errors and SatZ. The effect of topography
245 was investigated by checking the relationship of geometric errors in the across-track direction
246 over terrain areas compared to relatively flat areas. The effect of latitudes and longitude was
247 determined by analyzing their relationship with measured shifts on the along-track and across-
248 track directions, respectively.

249 **4 Results and discussions**

250 Fig. 4 shows the correlation distribution over the 33×33 shifted cases within ± 8 km range
251 at a step change of 500 m. Here, only one patch is extracted from each respective scene to



252 illustrate the results. Each grid in Fig. 4 represents a shift combination case, which is indicated
253 by the location of the grid away from the center. Then the geolocation errors can be transferred
254 into distances in kilometer (km) by multiplying the location of a grid with 500 m. The center
255 of each subfigure depicts the case in which the location of the patch on the reference scene is
256 exactly overlapped with that on the AVHRR scene. The results are visualized for one example
257 showing the spatial distribution of correlation between the MODIS reference scene and the
258 AVHRR data (Fig. 4). The color coding indicates a high correlation in dark green and reddish-
259 white colors indicate low correlation values. An almost perfect match is shown in Fig. 4b, where
260 the dark green area is nearly centered at the coordinates (0, 0). From Fig. 4a, it can be found
261 that the patch on the NOAA-17 scene shows geolocation errors of -1 km and 0 km in the along-
262 track and across-track directions, respectively. The Fig. 4b indicates a geolocation error of 0
263 km and -0.5 km in the along-track and across-track directions respectively for the patch on the
264 MetOp-A scene. And Fig. 4c indicates that the patch on the MetOp-B scene shows a geometric
265 error of 2 km in the along-track direction and -5.5 km in the across-track direction. However,
266 these figures show only the results of one single patch. The final results are based on a large
267 number of samples to be statistically significant.



268
269 **Figure 4.** Variations of the correlation with respect to each shift combination. Only the results of one
270 patch from the NOAA-17 (left), MetOp-A (middle), and MetOp-B (right) scenes are shown for
271 conciseness.

272 4.1 Geocoding accuracy

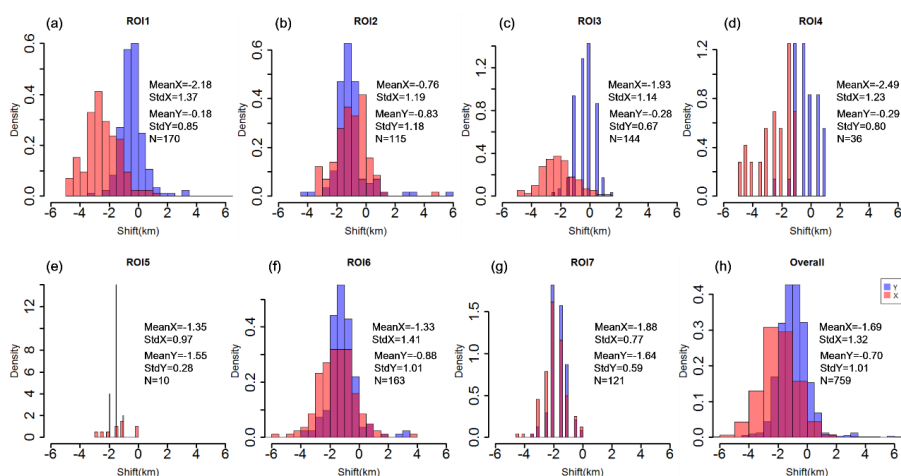
273 The geolocation shifts of each patch are slightly different as shown in Figs. 5-7. The +y
274 indicates a shift to the North and +x indicates a shift to the East (minus sign indicates opposite
275 directions). The statistical indicators such as the mean value of shift (Mean), the standard
276 deviation of shift (StdDev) and the number of patches (N), are derived from the estimated shift
277 values of all patches within the extent of the corresponding ROI.

278 As shown in Fig. 5, it can be seen that the scene of NOAA-17 generally shows West shifts
279 in the across-track direction, since the majority of patches in all ROIs show negative shifts.
280 Nevertheless, the magnitudes of shifts for different ROIs vary from one to another. ROI 2 shows
281 the smallest shift with a mean value of -0.76 km, with most shifts concentrated around -1 (Fig.



282 5b). The ROIs 6 and 5 indicate the second smallest shifts, with still weak magnitudes of -1.33
 283 and -1.35, respectively. Most of their shifts are distributed between -2 and 0 (Figs. 5f and e).
 284 The ROIs 7, 3, 1, 4 show slightly larger mean shifts but are still with the magnitudes of less
 285 than 2.5 km. These results are unexpected, because the ROIs (ROIs 2 and 6) over terrain areas
 286 are with smaller shifts than those (ROIs 7, 3, 1, 4) over relatively flat areas in the across-track
 287 direction. One possible reason is that the SatZ for ROIs 2 and 6 are not large (less than 40°)
 288 (Fig. 1b) so that the terrain effect on geolocation accuracy is counterbalanced by the small SatZ.
 289 This also indicates that the influence of small SatZ may be stronger than the terrain effect. But
 290 it is surprising that the ROI 7 (Fig. 5g), which is located at the nadir area (Fig. 1b), shows even
 291 larger shifts than other ROIs (ROIs 2, 6 and 5) with relatively larger SatZ. On the other hand,
 292 ROI 7 shows the most stable behavior, indicated by the smallest StdDev of 0.77. Other ROIs
 293 present relatively large, but still acceptable variations with StdDev ranging from 0.97 to 1.41
 294 (Figs. 5a-g).

295 When combining the results of all ROIs together (Fig. 5h), the shifts in the across-track
 296 direction generally follow an approximately normal distribution with a mean value of -1.69 and
 297 a standard deviation of 1.32. Nearly 91% of the shifts are within the range of ± 3 km, and the
 298 great majority (97%) of the shifts lay within a range of ± 4 km. The number of patches (N=759)
 299 is assumed to be sufficient to ensure reliability and robustness of the results and the reduction
 300 of the influence of random factors.



301
 302 **Figure 5.** The distribution of shifts in the across-track (X) and along-track (Y) directions over different
 303 regions for NOAA-17 scene. The unit of the shift is km.

304 The shifts in the along-track direction are mainly negative throughout these ROIs,
 305 indicating that the NOAA-17 scene is dominated by South shifts in the along-track direction.
 306 Nevertheless, a considerable number of patches also show slight North shifts over ROIs 1, 3
 307 and 4 (Figs. 5a, c and d), where the shifts are distributed around 0 with mean values of -0.18, -



308 0.28 and -0.29, respectively. These shifts are generally small in these three regions given that
 309 the maximum shift is no more than 3.5 km (Table 2). In contrast, the ROIs 2, 5, 6 and 7 present
 310 systematic shifts to the South, which are mostly distributed within the range of -2 to 0 km, with
 311 mean values of -0.83, -1.55, -0.88 and -1.64, respectively (Figs. 5b, e, f and g). The large
 312 differences in the distribution of shifts over different ROIs demonstrate that the shifts in the
 313 along-track direction are dependent on the region. It is interesting to find that ROI 7 still shows
 314 the smallest StdDev of 0.59 when excluding ROI 5 due to its very small number of patches.
 315 This indicates that ROI 7 also shows the smallest uncertainty in the along-track direction. And
 316 this may be associated with its smallest SatZ among all investigated ROIs. When combining
 317 the results of different ROIs (Fig. 5h), the overall shifts in the along-track direction
 318 approximately obey a normal distribution, with an average of -0.70 and a standard deviation of
 319 1.01. Nearly 70% of them are within the range of ± 1 km, and only a small part (1.5%) show
 320 values larger than 3 km.

321 Furthermore, it can be stated that the distribution of shifts in the along-track direction is
 322 less widely spread than that in the across-track direction, demonstrating the smaller uncertainty
 323 of geocoding in the along-track direction, as indicated by the smaller StdDev values throughout
 324 these ROIs (Table 2). Moreover, the geolocation errors in the across-track direction are greater
 325 than the along-track direction (Fig. 5), which is expected due to the applied clock drift
 326 correction.

327 **Table 2.** Summary of the results for the scene of NOAA-17. The unit of the shift is km.

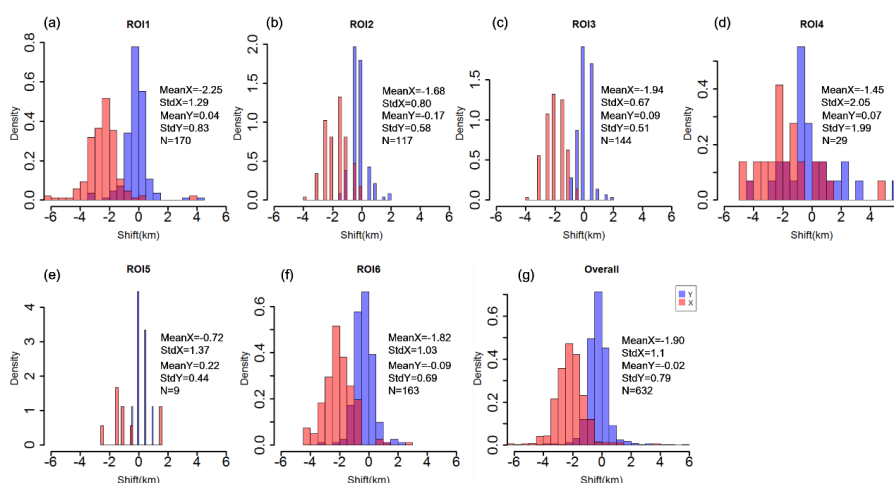
ROI	Min(X)	Max(X)	Mean(X)	StdDev(X)	Min(Y)	Max(Y)	Mean(Y)	StdDev(Y)	N
1	-5	7	-2.18	1.37	-3.5	3.5	-0.18	0.85	170
2	-3.5	5	-0.76	1.19	-4.5	6	-0.83	1.18	115
3	-5	1.5	-1.93	1.14	-2.5	1.5	-0.28	0.67	144
4	-5	-1	-2.49	1.23	-2.5	1	-0.29	0.80	36
5	-3	0	-1.35	0.97	-2	-1	-1.55	0.28	10
6	-7.5	4	-1.33	1.41	-4	3.5	-0.88	1.01	163
7	-4.5	0	-1.88	0.77	-3.5	0	-1.64	0.59	121
Overall	-7.5	7	-1.69	1.32	-4.5	6	-0.70	1.01	759

328 Similar to the results of NOAA-17, MetOp-A scene mainly present West shifts in the
 329 across-track direction, indicated by the widely distributed negative values throughout these
 330 ROIs (Figs. 6a-f). These shifts are basically concentrated around -2, however, the ROIs 2 and
 331 6 located in the terrain areas, show smaller average shifts (-1.68 and -1.82, respectively) than
 332 those of ROIs 1 and 3 (-2.25 and -1.94, respectively) over the relatively flat areas. This is
 333 understandable since the ROIs 2 and 6 are closer to the nadir area (Fig. 1d). And this align with
 334 the results from NOAA-17, where the influence of SatZ is also stronger than the terrain effect.
 335 Although the ROIs 5 and 4 show the smallest average shifts (-0.72 and -1.45, respectively) in
 336 the across-track direction, their results may be biased due to the smaller number of analyzed
 337 patches. It is interesting to find that ROI 3, which is almost located in the nadir area, still shows
 338 the least uncertainty, indicated by the smallest StdDev of 0.67. Furthermore, all ROIs close to
 339 the nadir area are characterized by small StdDevs (0.8 and 1.03 for ROIs 2 and 6, respectively)



340 compared to ROIs located further away from the nadir area (1.29, 2.05, 1.37 for ROIs 1, 4, 5,
 341 respectively). These results demonstrate that SatZ plays a crucial role in determining the
 342 uncertainty of the shifts in the across-track direction. This conclusion also agrees with previous
 343 research conducted by Aguilar et al. (2013). When combining the results of all ROIs (Fig. 6g),
 344 the shifts approximately follow a normal distribution, with an average of -1.90 and a standard
 345 deviation of 1.1. Most of the patches (94%) are within the range of ± 3 km, and nearly 98% of
 346 them are with shifts less than ± 4 km.

347 Since ROIs 1-6 on the MetOp-A scene are identical to those on NOAA-17 scene in terms
 348 of spatial extents, their shifts in the across-track direction are generally comparable. When
 349 excluding the results of ROIs 4 and 5, the ROIs on the MetOp-A scene generally show larger
 350 average shifts but smaller StdDevs than the NOAA-17 scene in the across-track direction (see
 351 Table 2 and 3). However, it does not necessarily mean that the MetOp-A scene has a smaller
 352 uncertainty than NOAA-17 scene in the across-track direction, because the ROIs on the MetOp-
 353 A scene are slightly closer to the nadir area than those on the NOAA-17 scene (Figs. 1b and d).
 354 Given the larger SatZ and the smaller average shifts of NOAA-17 scene, it is reasonable to
 355 conclude that the NOAA-17 scene shows a slightly better geolocation accuracy than the
 356 MetOp-A scene in the across-track direction.



357
 358 **Figure 6.** The distribution of shifts in the across-track (X) and along-track (Y) directions over different
 359 regions for MetOp-A scene. The unit of the shift is km.

360 Looking at the shifts in the along-track direction, the MetOp-A scene does not show strong
 361 systematic North or South shifts, but rather a general distribution of the shifts around 0 (Figs.
 362 6a-f). The shifts are generally small within a range of ± 1 km, with StdDevs less than 0.83
 363 except for ROI 4. Furthermore, ROIs 2, 3 and 6 that are located close to the nadir area exhibit
 364 smaller StdDevs than those located further away from the nadir area when excluding ROI 5 due
 365 to its very small number of patches. This further indicates that SatZ also determines the



366 uncertainty of shifts in the along-track direction. When combining the results of all ROIs (Fig.
 367 6g), the shifts also display a nearly normal distribution, with an average of -0.02 and a StdDev
 368 of 0.79. Nearly 94% of the shifts are within the range of ± 1 km and almost all of them (98%)
 369 are distributed within the range of ± 2 km. It can be found that the shifts in the along-track
 370 direction are obviously smaller and more centralized than those in the across-track direction.
 371 This can be further confirmed by the consistently smaller StdDev values in the along-track
 372 direction than those in the across-track direction as shown in Table 3.

373 **Table 3.** Summary of the results for the scene of MetOp-A. The unit of the shift is km.

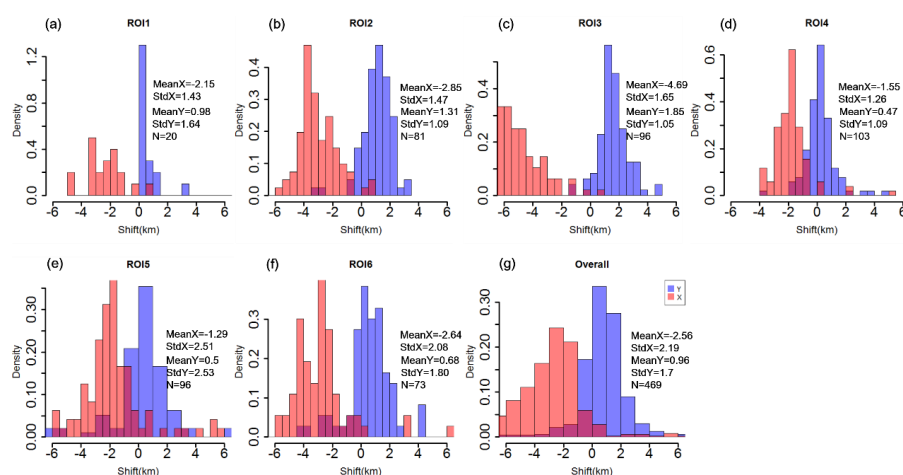
ROI	Min(X)	Max(X)	Mean(X)	StdDev(X)	Min(Y)	Max(Y)	Mean(Y)	StdDev(Y)	N
1	-7	4	-2.25	1.29	-3.5	4.5	0.04	0.83	170
2	-4	0	-1.68	0.80	-1.5	2	-0.17	0.58	117
3	-4	-0.5	-1.94	0.67	-1	2	0.09	0.51	144
4	-5	5	-1.45	2.05	-4.5	6	0.07	1.99	29
5	-2.5	1.5	-0.72	1.37	-0.5	1	0.22	0.44	9
6	-4.5	3	-1.82	1.03	-3.5	2.5	-0.09	0.69	163
Overall	-7	5	-1.90	1.10	-4.5	6	-0.02	0.79	632

374 By comparing Figs. 6a-f with Figs. 5a-f, it becomes obvious that large differences exist
 375 between the shifts in the along-track direction of MetOp-A and NOAA-17 scenes. In the first
 376 place, systematic South shifts occur on the NOAA-17 scene but not on the MetOp-A scene.
 377 Secondly, the magnitudes of shifts on the MetOp-A scene are generally smaller than those on
 378 the NOAA-17 scene, as the former are concentrated around 0 while the latter are concentrated
 379 around -1. Thirdly, the distribution of shifts is more centralized for the MetOp-A scene
 380 compared to the NOAA-17 scene, except for ROIs 4 and 5. This can further be proved by the
 381 smaller StdDev values for MetOp-A (Table 3) than those for NOAA-17 (Table 2). Therefore, it
 382 can be concluded that the MetOp-A scene shows a better geolocation accuracy and less
 383 uncertainty than the NOAA-17 scene in the along-track direction.

384 Similar to the scenes of NOAA-17 and MetOp-A, the MetOp-B scene generally shows
 385 West shifts in the across-track direction, indicated by the predominant occurrence of negative
 386 values (Figs. 7a-f). Nevertheless, unlike the results for the terrain areas on NOAA-17 and
 387 MetOp-A scenes, the ROI 3 located in the terrain area on the MetOp-B scene (Fig. 2a), shows
 388 the largest shifts throughout these ROIs with an average of -4.69 in the across-track direction.
 389 Furthermore, the magnitudes of these shifts are characterized by even larger values than 6 km
 390 (Fig. 7c). This is most probably caused by the combined effect of topography and large SatZ
 391 (Fig. 2b). Significant terrain effects appear only in the case of SatZ larger than 40° as shown in
 392 Fig. 2b. This finding agrees with the previous study by Fontana et al. (2009), who demonstrated
 393 that the errors in across-track direction result from the intertwined effects of observation
 394 geometry and terrain elevation. Nevertheless, ROI 5 that is located in the nadir area (Fig. 2d),
 395 shows the smallest average shift of -1.29 but the largest standard deviation of 2.51 (Fig. 7e).
 396 The largest StdDev is attributed to the fact that a considerable number of shifts exhibit values



397 of ± 6 km. As shown in Fig. 2c, the main reason for these large and unstable shifts may be the
398 presence of thin clouds or cloud shadows in this region. By comparing the results of ROIs 4
399 and 5 with smaller SatZ against ROIs 2, 3, 6 with larger SatZ (Figs. 2b and d), it can be stated
400 that the shifts with smaller SatZ are generally weaker than those with larger SatZ (Figs. 7b-f).
401 When combining the results of all ROIs (Fig. 7g), the MetOp-B scene shows an average shift
402 of -2.56 km with a standard deviation of 2.19 in the across-track direction. Only 63% of the
403 shifts are distributed within the range of ± 3 km, and the percentage raises up to 92% within
404 the range of ± 5.5 km.



405

406 **Figure 7.** The distribution of shifts in the across-track (X) and along-track (Y) directions over different
407 regions for MetOp-B scene. The unit of the shift is km.

408 Since the extent of the ROIs in the MetOp-B scene are not consistent with those on NOAA-
409 17 and MetOp-A scenes, only their overall performances in the across-track direction are
410 compared here. By comparing Fig. 7g with Fig. 6g and Fig. 5h, it is obvious that the MetOp-B
411 scene shows larger shifts and greater uncertainties than NOAA-17 and MetOp-A scenes in the
412 across-track direction. This is partly due to the larger range of SatZ of these ROIs and partly
413 due to the worse geolocation accuracy of the MetOp-B scene in the across-track direction.

414 The MetOp-B scene is dominated by North shifts in the along-track direction, indicated
415 by the predominantly positive shift values (Figs. 7a-f). It is interesting to find that ROI 3, which
416 is located at terrain area and with large SatZ, shows the largest shifts with an average of 1.85
417 km in the along-track direction. Given that terrain does not affect the geolocation accuracy in
418 the along-track direction, the main cause of the largest shift may be the largest SatZ of ROI 3
419 among these ROIs. Furthermore, by comparing the results of ROI 4 and 5 with those of ROI
420 2, 3, 6, it can be found the shifts of ROIs with smaller SatZ are more concentrated around 0
421 (Figs. 7d and e), while the shifts of ROIs with larger SatZ are more widely spread (Figs. 7b, c,
422 and f). This manifests that the effect of large SatZ on shifts in the along-track direction cannot



423 be neglected. When combining the results of all ROIs, the MetOp-B scene shows shifts with an
 424 average of 0.96 and a standard deviation of 1.7. Only 52% of the shifts are distributed within
 425 the range of ± 1 km, and the percentage raises up to 92% for the range of ± 3 km.

426 It can be seen that the shifts in the along-track direction are still significantly smaller than
 427 those in the across-track direction. Furthermore, the uncertainties of the shifts in the along-track
 428 direction are generally smaller than those in the across-track direction, when excluding the
 429 results of ROI 1 due to its limited number of patches (Table 4). This further verifies that after
 430 removing clock drift errors, the geolocation errors in the along-track direction are generally
 431 more accurate and with less uncertainties than the across-track direction.

432 **Table 4.** Summary of the results for the scene of MetOp-B. The unit of the shift is km.

ROI	Min(X)	Max(X)	Mean(X)	StdDev(X)	Min(Y)	Max(Y)	Mean(Y)	StdDev(Y)	N
1	-5	1	-2.15	1.43	0	7	0.98	1.64	20
2	-7.5	1	-2.85	1.47	-3.5	3.5	1.31	1.09	81
3	-7.5	1	-4.69	1.65	-1.5	5	1.85	1.05	96
4	-4	5.5	-1.55	1.26	-4	5	0.47	1.09	103
5	-6	7.5	-1.29	2.51	-7.5	7.5	0.50	2.53	96
6	-7.5	6.5	-2.64	2.08	-7	4.5	0.68	1.80	73
Overall	-7.5	7.5	-2.56	2.19	-7.5	7.5	0.96	1.70	469

433 The comparison of Fig. 7g with Fig. 6g and Fig. 5h reveals that the MetOp-B scene is
 434 significantly inferior to the MetOp-A scene in terms of the geolocation accuracy in the along-
 435 track direction, with the former being concentrated around 1 and the latter around 0.
 436 Furthermore, the uncertainty of the shifts of the MetOp-B scene (StdDev=1.7) is much larger
 437 than that of the MetOp-A scene (StdDev=0.79). As for the performance of the MetOp-B scene
 438 relative to the NOAA-17 scene, it can be found that they are comparable with regard to the
 439 magnitude as well as the distribution of the shifts in the along-track direction. However, the
 440 MetOp-B scene shows larger uncertainties than NOAA-17.

441 From the results above, it can be concluded that NOAA-17 and MetOp-A scenes show
 442 distinct advantages over the MetOp-B scene in both directions. However, the NOAA-17 scene
 443 is slightly better than the MetOp-A scene in the across-track direction, with average shifts of -
 444 1.69 for NOAA-17 and -1.90 for MetOp-A, which are both greatly lower than for MetOp-B (-
 445 2.56). But the MetOp-A scene shows a distinct advantage over NOAA-17 in the along-track
 446 direction, with an average shift of -0.02 for MetOp-A and -0.7 for NOAA-17, which are both
 447 lower than for MetOp-B (0.96). In addition to the magnitudes of their shifts, the MetOp-B scene
 448 also shows larger uncertainties than NOAA-17 and MetOp-A scenes in both directions.

449 4.2 The potential influence factors

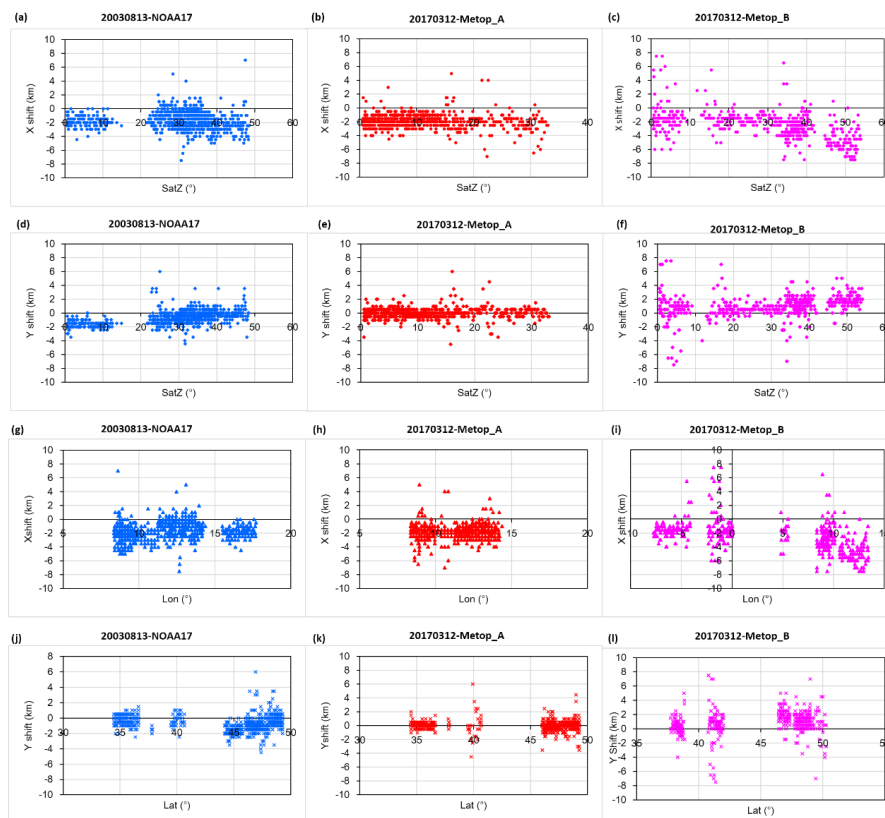
450 From the above results, it is known that SatZ plays an important role in determining the
 451 geolocation accuracy of the satellite scene. To investigate how and to what extent it influences
 452 the geolocation accuracy, Fig. 8 displays the shifts in both directions as a function of SatZ for
 453 all three satellites. Furthermore, the influences of latitude and longitude on geolocation



454 accuracy are also explored.

455 As shown in Figs. 8a-c, it can be seen that the shifts in the across-track direction vary
456 considerably for all SatZ, and this is particularly evident in the results of MetOp-B (Fig. 8c).
457 This demonstrates that besides the SatZ effects, the geolocation accuracy is also influenced by
458 other factors. Furthermore, the spread at each fixed SatZ tends to become larger at larger SatZ
459 (larger than 20°) (Figs. 8a-b). The large variability of MetOp-B scene shifts at small SatZ (less
460 than 20°) (Fig. 8c) is mainly due to the effect of thin cloud or cloud shadow as explained before.
461 Despite the dispersion of the shifts for all SatZ, it can still be found that the shifts in the across-
462 track direction do not change much when the SatZ is less than 20° (Figs. 8a-b and Table 5). A
463 slightly decreasing trend (increasing trend of the magnitude) can be observed from 20° to 40°
464 (Table 5), and becomes more apparent at SatZ larger than 40° (Fig. 8c and Table 5).
465 Furthermore, it can be found that for small SatZ (less than 20°) the shifts in the across-track
466 direction are generally concentrated around 2 km for NOAA-17 and MetOp-A scenes (Figs. 8a-
467 b). With increasing SatZ, the largest magnitudes of shifts become larger but basically stay
468 within the range of 4 km for SatZ smaller than 40°. For even larger SatZ (larger than 40°), the
469 magnitude of shifts can reach 6 km for NOAA-17 scene and 8 km for MetOp-B scene. From
470 these results, it can be inferred that the SatZ has a considerable effect on both the magnitude
471 and uncertainty of the shifts in across-track direction. The larger SatZ generally contributes to
472 larger shifts and uncertainties in the across-track direction. Furthermore, it can be inferred that
473 the GAC data with SatZ less than 40° should be preferred in applications.

474 Compared to the shifts in the across-track direction (Figs. 8a-c), the shifts in the along-
475 track direction show smaller variability at each fixed SatZ (Figs. 8d-f). From Figs. 8d-e, it can
476 be seen that the shifts in the along-track direction are relatively stable at each level of SatZ for
477 SatZ smaller than 15°, but becomes more variable for greater SatZ. A similar phenomenon can
478 be observed in Fig. 8f, where the shifts are relatively stable with SatZ ranging from 20° to 35°,
479 but becomes more variable at each level of SatZ with its values larger than 35°. It is noteworthy
480 that the wide spread of shifts with SatZ less than 20° is mainly caused by cloud contamination.
481 These results confirm the influence of larger SatZ on the uncertainty of shifts in the along-track
482 directions. It is interesting to find that the magnitudes of NOAA-17 scene shifts with small SatZ
483 (less than 20°) are even larger than those with larger SatZ (larger than 20°) (Fig. 8d). On the
484 contrary, the magnitudes of MetOp-B scene shifts with smaller SatZ (20-35°) are smaller than
485 those with larger SatZ (larger than 35°) (Fig. 8f). Nevertheless, all three sensors have in
486 common that they do not show clear change with SatZ smaller than 20° for NOAA-17 and
487 smaller than 35° for MetOp-A and MetOp-B (Figs. 8d-f). For larger SatZ than these values,
488 shifts exhibit a slightly decreasing trend for NOAA-17 (Fig. 8d) and an increasing trend for
489 MetOp-B (Fig. 8f). From these results, it can be stated that the influences of large SatZ on the
490 magnitude of shifts in the along-track direction are probably intertwined with other factors.



491
 492 **Figure 8.** Influence of SatZ (a-c), longitude (d-f), and latitude (g-i) on the geolocation results of NOAA-
 493 17 (left), MetOp-A (middle) and MetOp-B (right) scenes.

494 **Table 5.** The mean shift for each range of SatZ in the across-track direction. The unit of the shift is km.

SatZ	0°-10°	10°-20°	20°-30°	30°-40°	40°-50°	50°-60°
NOAA-17	-1.84	-1.84	-1.32	-1.66	-2.27	
MetOp-A	-1.87	-1.80	-2.06	-2.62		
MetOp-B	-1.29	-1.45	-1.75	-2.71	-3.95	-4.93

495 From Figs. 8g-i, it can be found that the variation of shifts (in the across-track direction)
 496 with longitude largely depends on the situation. For NOAA-17, the shifts tend to be smaller
 497 with the longitudinal range of 10°-15° and become larger outside this range (Fig. 8g). The
 498 MetOp-A scene does not show apparent change with longitude between 8° and 15° and neither
 499 does MetOp-B within the range of -8°-0°. However, MetOp-B presents a clear decreasing trend
 500 (an increasing trend in magnitude) for longitudes larger than 5°. Given the fact that the latitude
 501 of the nadir area is distributed between 10°-15° for NOAA-17, 8°-15° for MetOp-A, and -8°-
 502 0° for MetOp-B (Figs. 1b and d, Figs. 2b and d), it can be concluded that the influence of
 503 longitude on the shifts in the across-track direction is related to the longitude of nadir area of



504 the satellite, as it shows almost no influence in the nadir area. The influence increases with the
505 difference of the longitude relative to that of the nadir area. This is well understandable, as the
506 influence of longitude is equivalent to that of SatZ in the across-track direction.

507 The variation of the shifts (in the along-track direction) with latitude also depends on the
508 situation (Figs. 8j-l). The magnitudes of shifts with larger latitude (larger than 45°) are generally
509 greater than those with smaller latitude (less than 40°) on the NOAA-17 (Fig. 8j) and MetOp-
510 B scene (Fig. 8l). This is not visible for the MetOp-A scene (Fig. 8k), where the shifts exhibit
511 almost no change with latitude. This can be attributed to the fact that the clock drift errors are
512 corrected more thoroughly for MetOp-A satellite than NOAA-17 and MetOp-B satellites.
513 Furthermore, the MetOp satellites have an on-board stabilization to keep them in the right
514 position and orientation in orbit compared to the NOAA satellites.

515 **5 Conclusions**

516 The geometric accuracy of satellite data is crucial for most applications as geometric
517 inaccuracy can bias the obtained results. Therefore, the assessment of the geolocation accuracy
518 is important to provide satellite data of high quality enabling successful applications. In this
519 study, a correlation-based patch matching method was proposed to characterize and quantify
520 the AVHRR GAC geo-location accuracy. This method presented here yields significant
521 advantages over existing approaches and enables achieving a subpixel geo-positioning accuracy
522 of coarse resolution scenes. It is free from the impact of false detection due to the influence of
523 mixed pixels, not limited to a certain landmark (e. g. shoreline) and therefore enables a more
524 comprehensive geometric assessment. This method was utilized to characterize the geolocation
525 accuracy of AVHRR GAC scenes from NOAA-17, MetOp-A, and MetOp-B satellites.

526 The study is based on several ROIs comprising numerous patches over different land cover
527 types, latitudes, and topographies. The scenes from these satellites all present West shifts in the
528 across-track direction, with an average shift of -1.69 km and a StdDev of 1.32 km for NOAA-
529 17, -1.9 km and 1.1 km respectively for MetOp-A, and -2.56 km and 2.19 km respectively for
530 MetOp-B. In regard to the shifts in the along-track direction, NOAA-17 generally shows South
531 shifts with an average of -0.7 km and a StdDev of 1.01 km. By contrast, the MetOp-B mainly
532 present North shifts with an average of 0.96 km and a StdDev of 1.70 km. The MetOp-A scene
533 shows a distinct advantage over NOAA-17 and MetOp-B in the along-track direction without
534 obvious shifts, indicated by the average of -0.02 km and a StdDev of 0.79 km. Generally, the
535 MetOp-B scene is inferior to NOAA-17 and MetOp-A scenes, with larger shifts and
536 uncertainties in both directions. Despite the variation of shifts due to various factors (e. g. SatZ,
537 topography), more than 90 percent of the AVHRR GAC data across-track errors are within \pm
538 3 km for NOAA-17 and MetOp-A, and ± 5.5 km for MetOp-B. Along-track errors are within
539 ± 2 km for NOAA-17, ± 1 km for MetOp-A, and ± 3 km for MetOp-B for more than 90
540 percent of the test data. It is important to note that since these satellites show different shifts,



541 using the combined data from NOAA-17 and MetOp will result in additional uncertainty in
542 time series applications.

543 From the results above, it can be found that the geolocation accuracy in the along-track
544 direction is always higher and with less uncertainties than the across-track direction, which is
545 consistent with previous related studies. This is understandable since the GAC dataset from the
546 ESA cloud CCI project has been corrected for clock drift errors, but has no ortho-correction,
547 which is not feasible due to the onboard sampling characteristics. SatZ plays a decisive role in
548 determining the magnitude as well as the uncertainty of the shifts in the across-track direction.
549 Larger SatZ generally induce greater shifts and uncertainties in this direction. The combined
550 effect of SatZ and topography on geolocation accuracy in the across-track direction has also
551 been shown. And significant terrain effects appear only in the case of large SatZ ($>40^\circ$ for this
552 study). It is important to note that the effect of SatZ on the magnitude and uncertainty of shifts
553 in the along-track direction is not negligible. But this effect is likely to be intertwined with other
554 factors. The impact of longitude on the shifts in the across-track direction is equivalent to that
555 of SatZ, while the effect of latitude is related to the degree of how the clock drift errors are
556 corrected. It was found that the clock drift errors are more thoroughly corrected for MetOp-A
557 than NOAA-17 and MetOp-B.

558 Although this assessment was only conducted for a single scene of each satellite, it
559 provides an important preliminary geolocation assessment for AVHRR GAC data. It is a first
560 step towards a more precise geolocation and thus improves application of coarse-resolution
561 satellite data. For instance, it identifies the threshold of SatZ under which the GAC data should
562 be preferred in applications. Furthermore, the CPMM geolocation assessment method proposed
563 by this study is also applicable to other coarse-resolution satellite data.

564 **Data availability**

565 The AVHRR GAC test data in this paper draw on datasets from ESA CCI cloud project
566 (<http://www.esa-cloud-cci.org/>) where is also the data availability indicated (Stengel et al.,
567 2017). And the MOD13A1 V006 data can be downloaded via
568 <https://ladsweb.modaps.eosdis.nasa.gov/> (Didan, 2015).

569 **Author contributions**

570 Xiaodan Wu was responsible for the main research ideas and writing the manuscript.
571 Kathrin Naegeli contributed to the data collection. Stefan Wunderle contributed to the
572 manuscript organization. All the authors thoroughly reviewed and edited this paper.

573 **Competing interests**

574 The authors declare that they have no conflict of interest.



575 **Acknowledgments**

576 The authors are grateful to the ESA CCI (Climate Change Initiative) cloud project team
577 (Dr. Martin Stengel, Dr. Rainer Hollmann) to make the data sets available for this study. This
578 work was supported by the National Natural Science Foundation of China (41801226).

579 **References**

- 580 Aguilar, M. A., del Mar Saldana, M., and Aguilar, F. J.: Assessing geometric accuracy of the
581 orthorectification process from GeoEye-1 and WorldView-2 panchromatic images, *Int. J. Appl.*
582 *Earth Obs.*, 21, 427-435, 2013.
- 583 Aksakal, S. K.: Geometric accuracy investigations of SEVIRI high resolution visible (HRV) level
584 1.5 Imagery, *Remote Sens.*, 5(5), 2475-2491, 2013.
- 585 Aksakal, S. K., Neuhaus, C., Baltasvias, E., and Schindler, K.: Geometric quality analysis of
586 AVHRR orthoimages, *Remote Sens.*, 7(3), 3293-3319, 2015.
- 587 Alcaraz - Segura, D., Chuvieco, E., Epstein, H. E., Kasischke, E. S., and Trishchenko, A.: Debating
588 the greening vs. browning of the North American boreal forest: differences between satellite
589 datasets, *Global Change Biol.*, 16(2), 760-770, 2010.
- 590 Arnold, G. T., Hubanks, P. A., Platnick, S., King, M. D., and Bennartz, R.: Impact of Aqua
591 misregistration on MYD06 cloud retrieval properties. In *Proceeding of MODIS Science Team*
592 *Meeting*, Washington, DC, USA, 26–28 January 2010.
- 593 Bicheron, P., Amberg, V., Bourg, L., Petit, D., Huc, M., Miras, B., ... and Leroy, M.: Geolocation
594 Assessment of MERIS GlobCover Orthorectified Products, *IEEE Trans. Geosci. Remote Sens.*,
595 49(8), 2972-2982, 2011.
- 596 Cihlar, J., Latifovic, R., Chen, J., Trishchenko, A., Du, Y., Fedosejevs, G., and Guindon, B.:
597 Systematic corrections of AVHRR image composites for temporal studies, *Remote Sens.*
598 *Environ.*, 89(2), 217-233, 2004.
- 599 Delbart, N., Le Toan, T., Kergoat, L., and Fedotova, V.: Remote sensing of spring phenology in
600 boreal regions: A free of snow-effect method using NOAA–AVHRR and SPOT–VGT data
601 (1982–2004), *Remote Sens. Environ.*, 101, 52–62, 2006.
- 602 Devasthale, A., Raspaud, M., Schlundt, C., Hanschmann, T., Finkensieper, S., Dybbroe, A., ... and
603 Karlsson, K. G.: PyGAC: an open-source, community-driven Python interface to preprocess
604 more than 30-year AVHRR Global Area Coverage (GAC) data, 2016.
- 605 Dietz, A. J., Frey, C. M., Ruppert, T., Bachmann, M., Kuenzer, C., and Dech, S.: Automated
606 Improvement of Geolocation Accuracy in AVHRR Data Using a Two-Step Chip Matching
607 Approach—A Part of the TIMELINE Preprocessor, *Remote Sens.*, 9(4), 303, 2017.
- 608 Didan, K.: MOD13A1 MODIS/Terra Vegetation Indices 16-Day L3 Global 500m SIN Grid V006
609 [Data set], NASA EOSDIS LP DAAC, doi: 10.5067/MODIS/MOD13A1.006,
610 <https://ladsweb.modaps.eosdis.nasa.gov/>, 2015.



- 611 D'Souza, G., and Malingreau, J. P.: NOAA - AVHRR studies of vegetation characteristics and
612 deforestation mapping in the Amazon Basin, *Remote Sens. Rev.*, 10(1-3), 5-34, 1994.
- 613 Fontana, F. M., Trishchenko, A. P., Khlopenkov, K. V., Luo, Y., and Wunderle, S.: Impact of
614 orthorectification and spatial sampling on maximum NDVI composite data in mountain
615 regions, *Remote Sens. Environ.*, 113(12), 2701-2712, 2009.
- 616 WMO, I., and UNEP, I.: Systematic observation requirements for satellite-based products for
617 climate-Supplemental details to the satellite-based component of the "Implementation Plan for
618 the Global Observing System for Climate in Support of the UNFCCC"[J]. Technical Report
619 GCOS-107, WMO/TD No 1338, 2006.
- 620 Hoffman, L. H., Weaver, W. L., and Kibler, J. F.: Calculation and accuracy of ERBE scanner
621 measurement locations, NASA Tech. Pap. Rep. NASA/TP-2670, 34 pp., NASA Langley
622 Research Center, Hampton, Virginia, 1987.
- 623 Hollmann, R., Merchant, C., Saunders, R., Downy, C., Buchwitz, M., Cazenave, A., Chuvieco, E.,
624 Defourny, P., Leeuw, G. de, Forsberg, R., Holzer-Popp, T., Paul, F., Sandven, S.,
625 Sathyendranath, S., Roozendaal, M. van, and Wagner W.: The ESA Climate Change Initiative:
626 satellite data records for essential climate variables, *B. Am. Meteorol. Soc.*, doi:
627 10.1175/BAMS-D-11-00254.1, 2013.
- 628 Hori, M., Sugiura, K., Kobayashi, K., Aoki, T., Tanikawa, T., Kuchiki, K., ... and Enomoto, H.: A
629 38-year (1978–2015) Northern Hemisphere daily snow cover extent product derived using
630 consistent objective criteria from satellite-borne optical sensors, *Remote Sens. Environ.*, 191,
631 402-418, 2017.
- 632 Khlopenkov, K. V., Trishchenko, A. P., and Luo, Y.: Achieving subpixel georeferencing accuracy in
633 the Canadian AVHRR processing system, *IEEE Trans. Geosci. Remote Sens.*, 48(4), 2150-
634 2161, 2010.
- 635 Kidwell, K. B.: NOAA Polar Orbiter Data (POD) User's Guide, November 1998 revision, 1998.
636 <http://www2.ncdc.noaa.gov/docs/podug/>
- 637 Lee, T. Y., and Kaufman, Y. J.: Non-Lambertian effects on remote sensing of surface reflectance and
638 vegetation index, *IEEE Trans. Geosci. Remote Sens.*, 24, 699–708, 1986.
- 639 Moreno, J. F., and Melia, J.: A method for accurate geometric correction of NOAA AVHRR HRPT
640 data, *IEEE Trans. Geosci. Remote Sens.*, 31(1), 204-226, 1993.
- 641 Moulin, S., Kergoat, L., Viovy, N., and Dedieu, G.: Global-scale assessment of vegetation
642 phenology using NOAA/AVHRR satellite measurements, *J. Climate*, 10, 1154–1170, 1997.
- 643 Pouliot, D., Latifovic, R., and Olthof, I.: Trends in vegetation NDVI from 1 km AVHRR data over
644 Canada for the period 1985–2006, *Int. J. Remote Sens.*, 30, 149–168, 2009.
- 645 Rosborough, G. W., Baldwin, D. G., and Emery, W. J.: Precise AVHRR image navigation, *IEEE*
646 *Trans. Geosci. Remote Sens.*, 32(3), 644-657, 1994.
- 647 Stengel, M., Stapelberg, S., Sus, O., Schlundt, C., Poulsen, C., Thomas, G., Christensen, M.,
648 Carbajal Henken, C., Preusker, R., Fischer, J., Devasthale, A., Willén, U., Karlsson, K.-G.,
649 McGarragh, G. R., Proud, S., Povey, A. C., Grainger, R. G., Meirink, J. F., Feofilov, A.,



- 650 Bennartz, R., Bojanowski, J. S., and Hollmann, R.: Cloud property datasets retrieved from
651 AVHRR, MODIS, AATSR and MERIS in the framework of the Cloud_cci project, Earth Syst.
652 Sci. Data, 9, 881-904, <https://doi.org/10.5194/essd-9-881-2017>, 2017.
- 653 Stengel, M., Sus, O., Stapelberg, S., Schlundt, C., Poulsen, C., Hollmann, R.: ESA Cloud Climate
654 Change Initiative (ESA Cloud_cci) data: Cloud_cci AVHRR-AM L3C/L3U
655 CLD_PRODUCTS v2.0, Deutscher Wetterdienst (DWD),
656 https://doi.org/10.5676/DWD/ESA_Cloud_cci/AVHRR-AM/V002, 2017
- 657 Stöckli, R., and Vidale, P. L.: European plant phenology and climate as seen in a 20 year AVHRR
658 land-surface parameter dataset, Int. J. Remote Sens., 25, 3303–3330, 2004.
- 659 Takagi, M.: Precise geometric correction for NOAA and GMS images considering elevation effects
660 using GCP template matching and affine transform, Proceedings of SPIE Conference on
661 Remote Sensing, Image and Signal Processing for Remote Sensing IX, pp.132-141, Vol. 5238,
662 Barcelona, Spain, 2004.
- 663 Van, A., Nakazawa, M., and Aoki, Y.: Highly accurate geometric correction for NOAA AVHRR
664 data, 2008.
665 [http://cdn.intechopen.com/pdfs/10391/InTech%20Highly accurate geometric correction for](http://cdn.intechopen.com/pdfs/10391/InTech%20Highly%20accurate%20geometric%20correction%20for%20noaa%20avhrr%20data.pdf)
666 [noaa avhrr data.pdf](http://cdn.intechopen.com/pdfs/10391/InTech%20Highly accurate geometric correction for noaa avhrr data.pdf)
- 667 Wang, L., Tremblay, D. A., Han, Y., Esplin, M., Hagan, D. E., Predina, J., Suwinski, L., Jin, X., and
668 Chen, Y.: Geolocation assessment for CrIS sensor data records. J. Geophys. Res. Atmos.,
669 118(22), 12-690, 2013.
- 670 Wolfe, R. E., Nishihama, M., Fleig, A. J., Kuyper, J. A., Roy, D. P., Storey, J. C., and Patt, F. S.:
671 Achieving sub-pixel geolocation accuracy in support of MODIS land science, Remote Sens.
672 Environ., 83(1-2), 31-49, 2002.
- 673 Wolfe, R. E., Lin, G., Nishihama, M., Tewari, K. P., Tilton, J. C., and Isaacman, A. R.: Suomi NPP
674 VIIRS prelaunch and on-orbit geometric calibration and characterization, J. Geophys. Res.
675 Atmos., 118, 11,508–11,521, 2013.